AGU PUBLICATIONS

JGR

Journal of Geophysical Research: Space Physics

RESEARCH ARTICLE
10.1002/2016JA022360

Key Points:
- Flow deceleration, field line bending, and field-aligned currents are found in the lunar wake
- Alfven wings are confirmed in the lunar wake
- Pressure gradients along the lunar wake and flow deceleration are the source for the lunar Alfven wings

Correspondence to:
H. Zhang,
hzhang@mail.iggcas.ac.cn

Citation:
Zhang, H., et al. (2016), Alfvén wings in the lunar wake: The role of pressure gradients, *J. Geophys. Res. Space Physics*, *121*, 10,698–10,711, doi:10.1002/2016JA022360.

Received 7 JAN 2016
Accepted 12 OCT 2016
Accepted article online 15 OCT 2016
Published online 5 NOV 2016

Alfvén wings in the lunar wake: The role of pressure gradients

H. Zhang[1,2], K. K. Khurana[3], M. G. Kivelson[3,4], S. Fatemi[5], M. Holmström[6], V. Angelopoulos[3], Y. D. Jia[3], W. X. Wan[1,2], L. B. Liu[1,2], Y. D. Chen[1,2], H. J. Le[1,2], Q. Q. Shi[7], and W. L. Liu[8]

[1]Key Laboratory of Earth and Planetary Physics, Institute of Geology and Geophysics, Chinese Academy of Sciences, Beijing, China, [2]Beijing National Observatory of Space Environment, Institute of Geology and Geophysics, Chinese Academy of Sciences, Beijing, China, [3]Department of Earth, Planetary, and Space Sciences, University of California, Los Angeles, California, USA, [4]Climate and Atmospheres and Space Sciences and Engineering Department, University of Michigan, Ann Arbor, Michigan, USA, [5]Space Sciences Laboratory, University of California, Berkeley, California, USA, [6]Swedish Institute of Space Physics, Kiruna, Sweden, [7]School of Space Science and Physics, Shangdong University at Weihai, Weihai, China, [8]School of Astronautics, Beihang University, Beijing, China

Abstract Strongly conducting or magnetized obstacles in a flowing plasma generate structures called Alfvén wings, which mediate momentum transfer between the obstacle and the plasma. Nonconducting obstacles such as airless planetary bodies can generate such structures, which, however, have so far been seen only in sub-Alfvénic regime. A novel statistical analysis of simultaneous measurements made by two ARTEMIS satellites, one in the solar wind upstream of the Moon and one in the downstream wake, and comparison of the data with results of a three-dimensional hybrid model of the interaction reveal that the perturbed plasma downstream of the Moon generates Alfvén wings in super-Alfvénic solar wind. In the wake region, magnetic field lines bulge toward the Moon and the plasma flows are significantly perturbed. We use the simulation to show that some of the observed bends of the field result from field-aligned currents. The perturbations in the wake thus arise from a combination of compressional and Alfvénic perturbations. Because of the super-Alfvénic background flow of the solar wind, the two Alfvén wings fold back to form a small intersection angle. The currents that form the Alfvén wing in the wake are driven by both plasma flow deceleration and a gradient of plasma pressure, positive down the wake from the region just downstream of the Moon. Such Alfvén wing structures, caused by pressure gradients in the wake and the resulting plasma slowdown, should exist downstream of any nonconducting body in a super-Alfvénic plasma flow.

1. Introduction

Strongly conducting or magnetized obstacles in a flowing plasma generate Alfvén wings in regions surrounding the obstacle. These structures develop where incompressible perturbations are imposed by field-aligned currents (FACs) closing through the conducting body [*Neubauer*, 1980; *Southwood et al*., 1980; *Kivelson et al*., 1997; *Linker et al*., 1998]. Magnetic field lines start to drape around the conducting obstacle as the flowing plasma decelerates and is diverted. Alfvén waves are triggered and propagate along the field lines away from the interaction region into the surrounding plasma on both poles of the obstacle at the Alfvén speed, $V_A = \sqrt{B^2/\mu_0\rho}$, where B is the field strength and ρ is the plasma mass density. The Alfvén waves carry FACs that connect the obstacle to the undisturbed plasma above and below the obstacle, helping transport momentum that serves to reaccelerate the slowed plasma around the obstacle [e.g., *Drell et al*., 1965; *Neubauer*, 1980]. In the rest frame of the obstacle, if the background plasma velocity is V and the background magnetic field is perpendicular to the flow, the Alfvén waves travel at a flare angle $\theta_A = \mathrm{atan}(1/M_A)$ to the background flow V, where M_A is the Alfvén Mach number ($MA = V/V_A$). For a sub-Alfvénic background flow, the flare angle is large ($M_A < 1$, and thus $\theta_A > 45°$). For example, the two Galilean moons of Jupiter: Ganymede and Io, are embedded inside the sub-Alfvénic plasma of the Jupiter's corotating magnetosphere and carry Alfvén wings easily identified from both Galileo observations [*Kivelson et al*., 1997; *Linker et al*., 1998] and magnetohydrodynamic (MHD) simulations [e.g., *Linker et al*., 1998; *Kopp and Ip*, 2002; *Jia et al*., 2009]. In Saturn's magnetosphere, the largest icy satellite Rhea was found to also carry Alfvén wings in the sub-Alfvénic magnetospheric plasma of Saturn [*Simon et al*., 2012]. Although Alfvén wings are usually discussed in sub-Alfvénic flows, M_A does not have to be smaller than 1 for Alfvén wings to form. It is natural for "folded-up" wings to form with $\theta_A < 45°$ when the flow is super-Alfvénic ($M_A > 1$) [*Ridley*, 2007], although

in this case, fast/slow mode waves, including shocks, may also be important in forming the structures in the plasma [*Neubauer*, 1980].

Plasma deceleration around a celestial body can occur in several ways. The most common ones include slowing and diversion of flow resulting from the presence of a significant internal magnetic field, the finite conductivity of the body itself or its ionosphere [*Drell et al*., 1965], and/or from ion pickup (ionization and charge exchange) [*Goertz*, 1980]. *Linker et al*. [1998] included finite conductivity, ion pickup, and intrinsic magnetic fields in their MHD model. They found that both finite conductivity and ion pickup provide current closure paths that contribute to the formation of Alfvén wings, but they did not evaluate the relative importance of the two effects. The model of *Linker et al*. showed that Alfvén wings can form whether or not the body has an intrinsic magnetic field. *Jia et al*. [2011] identified an Alfvén wing structure at Enceladus, one of Saturn's moons embedded within the corotating saturnian magnetosphere, showing that closure currents produced by ion-pickup and the associated Alfvén wing structure are rotated by pickup of negatively charged dust.

Nonconducting, unmagnetized obstacles are generally thought not to generate Alfvén wings. The barren Moon, a particularly accessible and electromagnetically simple celestial body in the solar system, provides an opportunity to study an obstacle-plasma interaction in the limit of low electrical conductivity. Traditionally, the Moon is not treated as a conducting obstacle because it has none of the three possible properties: finite conductivity, a global intrinsic magnetic field, or a significant atmosphere (ionosphere) [*England et al*., 1968; *Sonett et al*., 1967; *Hoffman et al*., 1973]; therefore, Alfvén wings are not expected at the Moon. Except for some particle reflection confirmed in recent years [*Saito et al*., 2008; *Halekas et al*., 2011], the Moon has been treated as an insulator that absorbs the incident solar wind impacting on its surface while allowing the interplanetary magnetic fields (IMF) lines to pass through its body [*Lyon et al*., 1967]. A region of perturbed solar wind plasma, referred to as the lunar wake [*Colburn et al*., 1967; *Ness et al*., 1967; *Halekas et al*., 2015], forms behind the Moon. The lunar wake extends along the direction of the solar wind to several tens of lunar radii (R_L = 1738 km) [e.g., *Clack et al*., 2004] and tapers off when the ambient solar wind plasma reenters and fills up the void [e.g., *Wang et al*., 2011; *Holmstrom et al*., 2012; *Xie et al*., 2013; *Halekas et al*., 2015]. Within the lunar wake, magnetic perturbations as well as plasma perturbations are present. Although the IMF passes through the Moon unimpeded, the field magnitude increases in the central wake and decreases in rarefaction regions that surround the wake through the wave-mediated current systems [*Colburn et al*., 1967; *Fatemi et al*., 2013; *Zhang et al*., 2014]. Such field magnitude variations in the wake are imposed by pressure gradient forces [e.g., *Khurana et al*., 2008]. Using theoretical analyses and simulations, *Vernisse et al*. [2013] systematically studied the interaction between stellar winds, whether super-Alfvénic or sub-Alfvénic, and highly resistive planetary bodies. They argued that diamagnetic currents, which arise from pressure gradients, are significant sources of magnetic perturbations in a lunar-type interaction. Using Cassini data, *Simon et al*. [2012] showed that Alfvén wing-type structures are present in the lunar-type interaction between the sub-Alfvénic magnetospheric plasma flow of Saturn and its moon, Rhea, and ascribed their presence to the diamagnetic currents resulting from plasma density gradients. In this work, we will show that the plasma pressure gradient in the wake slows down the plasma entering into the wake. In response, an Alfvén wing current system gets established and helps reaccelerate the wake plasma to the ambient solar wind speed.

Satellite observations as well as simulations have noted field line bends and plasma deceleration that can be taken as clues for the presence of Alfvén wings in the lunar wake. However, bends and deceleration can be imposed in many ways, and the perturbations have not been identified as Alfvénic structures. Moonward magnetic field line bending has been noted in satellite observations [e.g., *Whang and Ness*, 1970; *Zhang et al*., 2014]. In hybrid simulations, moonward field line bends were found in the lunar wake [*Holmstrom et al*., 2012]. *Wang et al*. [2011] assumed that the Moon has a finite conductivity and attributed the moonward bends of field lines in their simulations to electric currents induced inside the Moon. We argue that field line bending caused by internal induction should decay with distance down the wake, but such decay is not supported by the ARTEMIS data [*Zhang et al*., 2014, Figure 10]. *Xie et al*. [2013] also found moonward field line bending in the lunar wake in their 3-D MHD simulation. They interpreted it as a consequence of a sunward pressure gradient force in the lunar wake. However, in their simulation the plasma is accelerated in the antisunward direction, which does not seem to be consistent with the moonward field line bends. Plasma flow deceleration, the other key feature of Alfvén wings, was identified in the lunar wake in the region where magnetic field lines bend toward the Moon [*Zhang et al*., 2014]. *Zhang et al*. [2014] suggested two candidate

mechanisms for the flow braking and associated Alfvén wing structures: the pickup effect of the heavy, charged lunar dust grains floating above the surface of the Moon, or the antimoonward plasma pressure gradient in the lunar wake, neither of which have been considered as a source of Alfvén wings.

In this paper, we investigate features of the lunar environment that are associated with Alfvén wings. The best way to diagnose perturbations as Alfvénic is to look for FACs, a unique feature of Alfvénic perturbations. Unfortunately, FACs cannot be measured by one or even two spacecraft, so we cannot infer their presence from ARTEMIS data. Consequently, we have built a three-dimensional hybrid model to identify Alfvénic features in the lunar wake and understand how Alfvén wings are excited. We conclude that an antisunward pressure gradient develops in the wake and is strong enough to slow the flow and impose the perturbations that form the Alfvén wings. We propose that Alfvén wings caused by pressure gradients and the attendant plasma slowdown should develop downstream of any nonconducting body in super-Alfvénic plasma flow as well as in sub-Alfvénic plasma [*Simon et al*., 2012; *Vernisse et al*., 2013].

The ARTEMIS observations are presented in the next section; simulation results, as well as a brief introduction to the 3-D hybrid simulation model, are presented in section 3; our interpretations are discussed in section 4. Section 5 provides our conclusions.

2. Observations

2.1. Instrumentation and Coordinate System

The data used in this study were obtained by the ARTEMIS mission, the extension of the Time History of Events and Macroscale Interactions during Substorms (THEMIS) mission; ARTEMIS consists of two identical satellites, P1 and P2 [*Angelopoulos*, 2011]. By design, when one probe traverses the lunar wake, the other orbits in the nearby solar wind, providing an opportunity to determine the lunar wake perturbations relative to unambiguously and accurately known solar wind and IMF conditions. Data from all of ARTEMIS's lunar wake crossings from 27 June 2011 to 3 June 2013 were used in this work, although data acquired in the near-Moon wake in regions of extremely low plasma density ($<0.1\ \mathrm{cm}^{-3}$) with large measurement uncertainty were discarded [*Zhang et al*., 2014]; about six million data points are used in this study. During the interval considered, the orbital periods of the two satellites are about 30 h, the apogee is near 12 R_L, and the perigee varies from several tens of kilometers to 0.5 R_L. The intersection angle between the main axes of the two satellite lunar orbits varies from ~30° to ~180°. The magnetic field and plasma data were obtained from the fluxgate magnetometer (FGM) [*Auster et al*., 2008] and a three-dimensional velocity distribution plasma instrument, the electrostatic analyzer [*McFadden et al*., 2008]. All the data are used at 3 s resolution, which is the spin period of spacecraft.

An orthogonal coordinate system with its origin set at the center of the Moon, the lunar solar magnetic system (LSM), is adopted to analyze perturbations relative to the directions of the IMF ($\vec{B}_{\mathrm{IMF}}$) and solar wind ($\vec{V}_{\mathrm{SW}}$). The X axis of the coordinate system points against the solar wind ($\hat{X} = -\vec{V}_{\mathrm{SW}}/|\vec{V}_{\mathrm{SW}}|$). The Y direction is defined by $\hat{Y} = -\hat{X}\times\vec{B}_{\mathrm{IMF}}/|\hat{X}\times\vec{B}_{\mathrm{IMF}}|$ when the angle between $\hat{X}$ and the IMF $\alpha = \arccos\left[\left(\hat{X}\cdot\vec{B}_{\mathrm{IMF}}\right)/|\vec{B}_{\mathrm{IMF}}|\right]$ is less than 90° and $\hat{Y} = \hat{X}\times\vec{B}_{\mathrm{IMF}}/|\hat{X}\times\vec{B}_{\mathrm{IMF}}|$ when $\alpha > 90°$. The Z direction completes the right-handed system by $\hat{Z} = \hat{X}\times\hat{Y}$. Thus, the background solar wind $\vec{V}_{\mathrm{SW}}$ is always along $-\hat{X}$ and the background IMF $\vec{B}_{\mathrm{IMF}}$ lies in the X-Z plane and always satisfies $B_{X,\mathrm{IMF}}B_{Z,\mathrm{IMF}} > 0$. Hereafter in the paper, we use θ_I, instead of $_\alpha$, to describe the inclination of the $\vec{B}_{\mathrm{IMF}}$ relative to $\hat{X}$, which is defined as $\theta_I = \alpha$ when $\alpha < 90°$ and $\theta_I = 180° - \alpha$ when $\alpha > 90°$. Clearly, θ_I always satisfies $0 < \theta_I < 90°$.

2.2. Case Studies

On 18 August 2011, from 15:13 UT to 16:10 UT, ARTEMIS P1 traversed the lunar wake (from $Z = -2$ to $Z = 2\ R_L$) near the $Y = 0$ plane in the LSM coordinate system ($|Y| < 0.5\ R_L$) in the near-Moon region ($0 > X > -2.4\ R_L$) (Figure 1a1). The Y coordinate varies because of change in the IMF, and the X coordinate varies mainly because of change in the solar wind speed (the X coordinate has been normalized by the instantaneous solar wind velocity (V_{SW}) to a velocity of 370 km/s; that is, the equivalent X is equal to $370X/V_{\mathrm{SW}}$). During the interval of the P1 wake crossing, ARTEMIS P2 was located in the nearby solar wind and observed an IMF inclination angle of $\theta_I = 54.9°$.

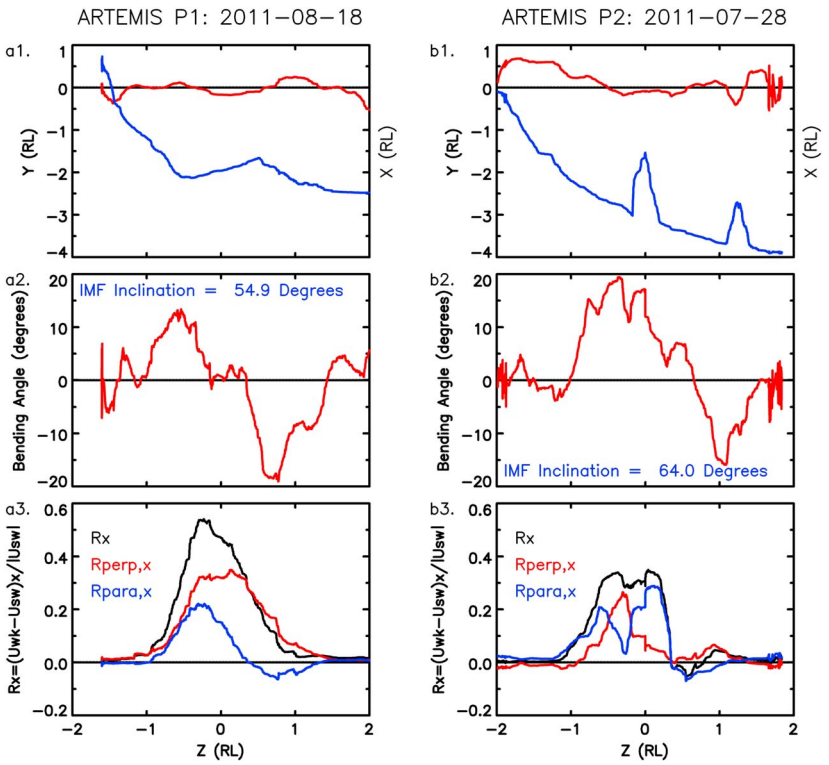

Figure 1. (a1–a3) The wake crossing event on 18 August 2011. The *X* (in blue) and *Y* (in red) coordinates of the observing satellite, P1, along its wake crossing orbit in unit of R_L as a function of the *Z* coordinate (Figure 1a1). The bend angle of magnetic field line δ_{XZ} (Figure 1a2). When $\alpha < 90°$ ($\alpha > 90°$), δ_{XZ} is defined as $\delta_{XZ} = \alpha - \alpha_{\text{Wake}}$ ($\delta_{XZ} = \alpha_{\text{Wake}} - \alpha$), where $\alpha = \arccos\left[\left(\hat{X}\cdot\vec{B}_{\text{IMF}}\right)/|\vec{B}_{\text{IMF}}|\right]$ is the intersection angle between the IMF and the *X* axis $\hat{X}$, $\alpha_{\text{Wake}} = \arccos\left[\left(\hat{X}\cdot\vec{B}_{XZ}\right)/|\vec{B}_{XZ}|\right]$ is the intersection angle of the *X* axis $\hat{X}$ and the magnetic field in the wake, and $\vec{B}_{XZ}$ is the projection of magnetic field vector in the wake into the *X*-*Z* plane. The *X* components of the plasma deceleration rate $\vec{R}$, $\vec{R}_{\text{perp}}$, and $\vec{R}_{\text{para}}$ plotted as a function of the *Z* coordinate (Figure 1a3). $\vec{R}$ is defined by the ratio $\vec{R} = \left(\vec{V}_{\text{WK}} - \vec{V}_{\text{SW}}\right)/|\vec{V}_{\text{SW}}|$, where $\vec{V}_{\text{SW}}$ is the background solar wind velocity and $\vec{V}_{\text{WK}}$ is the plasma velocity in the lunar wake. $\vec{R}_{\text{perp}}$ and $\vec{R}_{\text{para}}$ are calculated by using the flow components in the directions perpendicular and parallel to the magnetic field ($\vec{R}_{\text{perp}} = \left(\vec{V}_{\text{WK}} - \vec{V}_{\text{SW}}\right)_{\text{perp}}/|\vec{V}_{\text{SW}}|$ and $\vec{R}_{\text{para}} = \left(\vec{V}_{\text{WK}} - \vec{V}_{\text{SW}}\right)_{\text{para}}/|\vec{V}_{\text{SW}}|$), respectively. (b1–b3) The wake crossing event on 28 July 2011, and the format is the same as in Figures 1a1–1a3.

Field line bending is one of the critical features of Alfvén wings. Field line bending is quantified by the rotation angle (bend angle) δ_{XZ} of the field lines in the lunar wake relative to the background IMF $\vec{B}_{\text{IMF}}$ in the solar wind-IMF plane, i.e., the *X*-*Z* plane. When $\alpha < 90°$ ($\alpha > 90°$), δ_{XZ} is defined as $\delta_{XZ} = \alpha - \alpha_{\text{Wake}}$ ($\delta_{XZ} = \alpha_{\text{Wake}} - \alpha$), where α is the intersection angle of the IMF and the *X* axis $\hat{X}$, and $\alpha_{\text{Wake}} = \arccos\left[\left(\hat{X}\cdot\vec{B}_{XZ}\right)/|\vec{B}_{XZ}|\right]$ is the intersection angle of the *X* axis $\hat{X}$ and magnetic field in the *X*-*Z* plane in the wake and $\rightarrow B_{XZ}$ is the projection of magnetic field vector in the wake into the *X*-*Z* plane. Viewed against the *Y* axis, the sign of δ_{XZ} (>0 or <0) indicates whether the wake field lines rotate anticlockwise or clockwise in the *X*-*Z* plane, respectively. The bend angles of field lines in the lunar wake in the event on 18 August 2011 is shown in Figure 1a2 as a function of the *Z* coordinate. In the region where $Z \sim -1.5\ R_L$, δ_{XZ} is negative. As *Z* increases, δ_{XZ} increases to a peak value of ~14° at $Z = -0.6\ R_L$. δ_{XZ} then gradually decreases and changes sign at $Z = 0.4\ R_L$. δ_{XZ} has a second dip around $Z = 1\ R_L$, and the magnitude of the perturbation is about 20°. The overall bipolar profile of δ_{XZ} along the *Z* direction indicates that the magnetic field lines in the lunar wake bend toward the Moon. Clearly, δ_{XZ} is approximately antisymmetric about $Z = 0$ in the *X*-*Z* plane.

Plasma flow deceleration is another critical feature of Alfvén wings. Flow perturbations are quantified by $\vec{R} = \left(\vec{V}_{\text{WK}} - \vec{V}_{\text{SW}}\right)/|\vec{V}_{\text{SW}}|$ in this study, where $\vec{V}_{\text{SW}}$ is the background solar wind velocity and $\vec{V}_{\text{WK}}$ is the

plasma velocity in the lunar wake. R_X, the X component of $\overrightarrow{R}$, calculated by using only the X components of the velocities $R_X = \left(\overrightarrow{V}_{WK} - \overrightarrow{V}_{SW}\right)_X / |\overrightarrow{V}_{SW}|$, is plotted in Figure 1a3 in black. Notice that the X components of both $\overrightarrow{V}_{SW}$ and $\overrightarrow{V}_{WK}$ are negative (i.e., along the $-X$ direction). A positive R_X implies plasma deceleration, and a negative R_X implies flow acceleration. Thus, the profile of R_X along the Z direction for this event (black curve in Figure 1a3) indicates that plasma is decelerated in the lunar wake ($R_X > 0$). The deceleration rate R_X is asymmetric about $Z = 0$ with a peak at $Z = -0.3\ R_L$. To investigate this asymmetry in Z, flow perturbations are decomposed into perpendicular and parallel components by using $\overrightarrow{R}_{perp} = \left(\overrightarrow{V}_{WK} - \overrightarrow{V}_{SW}\right)_{perp} / |\overrightarrow{V}_{SW}|$ and $\overrightarrow{R}_{para} = \left(\overrightarrow{V}_{WK} - \overrightarrow{V}_{SW}\right)_{para} / |\overrightarrow{V}_{SW}|$, where the subscripts "perp" and "para" denote the components in the directions perpendicular and parallel to the magnetic field, respectively. The X components of $\overrightarrow{R}_{perp}$ and $\overrightarrow{R}_{para}$ are plotted in Figure 1a3 as red ($R_{perp,X}$) and blue ($R_{para,X}$) curves. It is seen that the perpendicular plasma flow is decelerated in the X direction throughout the wake crossing ($R_{perp,X} > 0$); the parallel flow, however, is decelerated in the X direction when $Z < 0$ ($R_{para,X} > 0$) and accelerated when $Z > 0$ ($R_{para,X} < 0$), thus accounting for the asymmetry of R_X. Both the plasma deceleration and the field line bending suggest that there is an Alfvén wing-type structure in the lunar wake.

Data from another wake crossing event on 28 July 2011, shown in Figures 1b1–1b3, also indicate the possible presence of Alfvén wings in the lunar wake. In this event, P2 crossed the lunar wake near the $Y = 0$ plane in the LSM coordinate system (Figure 1b1) and ARTEMIS P1, located in the nearby solar wind, observed an IMF inclination angle of about $\theta_I = 64°$. The downstream distance of this wake crossing ranges from 2.0 to 3.8 R_L, which is about 1 R_L more distant from the Moon than the event on 18 August 2011. Within the range $1 \geq Z \geq -1\ R_L$, the profile of the bend angle δ_{XZ} along the Z direction is again bipolar (Figure 1b2) corresponding to a Moonward bulge of field lines in the wake. The maximum bend angle for this event is larger than that of the event closer to the Moon discussed previously. Plasma is decelerated in the lunar wake ($R_X > 0$) and is accelerated slightly only in the positive Z region ($R_X < 0$ around $Z = 0.5\ R_L$) due to the acceleration of the parallel flows ($R_{para,X} < 0$). However, as contrasted with the previous case (the maximum R_X~0.5), the maximum R_X for this case is about 0.35 and the plasma deceleration decreases with distance downstream of the moon.

2.3. Statistical Studies

From June 2011 to June 2013, P1 or P2 observed more than 600 lunar wake crossings at downstream distances ranging from 0 to 12 R_L. The wide spatial range of wake crossings allows us to investigate the global field and plasma structure in the lunar wake, that is the distributions of the magnetic field bend angle δ_{XZ} and the plasma deceleration R with distance along the wake. The statistics of these observations are shown in Figure 2.

The lunar wake region is identified by perturbations of the solar wind ion number density. Figure 2a1 shows the distributions of the normalized ion densities N_{ion}/N_{SW} in the X-Z plane, where N_{ion} and N_{SW} are ion number densities near the Moon and in the solar wind, respectively. The Y and Z coordinates of each data point are the original observation locations in units of R_L. The length of the lunar wake, however, is sensitive to the solar wind speed (the faster the solar wind, the longer the lunar wake) [*Holmstrom et al*., 2012]. To correct for this source of variability, the X coordinate of each data point is normalized by multiplying the ratio of the instantaneous solar wind velocity (V_{SW}) to the average solar wind velocity (370 km/s); that is, the equivalent X is equal to $370X/V_{SW}$. In all panels, the white circle indicates the solar wind shadow boundary, and the oblique lines or curves mark the locations of the wavefront s of three MHD modes (red indicates the fast mode, black indicates the Alfvén mode, and blue indicates the slow mode) launched at the lunar terminator and propagating at their group velocities in the solar wind. These front locations are calculated on the basis of the median solar wind properties in our data set; the background solar wind density, temperature, and velocity are 6.6 cm^{-3}, 9.46 eV, and 370 km/s, respectively, corresponding to a 69 km/s sonic velocity and a 64 km/s Alfvén velocity; the background IMF is 4.9 nT with an inclination angle θ_I about 58°. In the Z direction, the locations of all the three MHD modes are close to each other, and it is hard to determine which front confines the density depletion region. Figures 2a2 and 2a3 display the bin-averaged ion densities in the Y-Z planes at different downstream distances. Because the Alfvén mode and slow mode propagate only along or nearly along the magnetic field direction, in terms of group velocities, the wavefronts of these two modes are

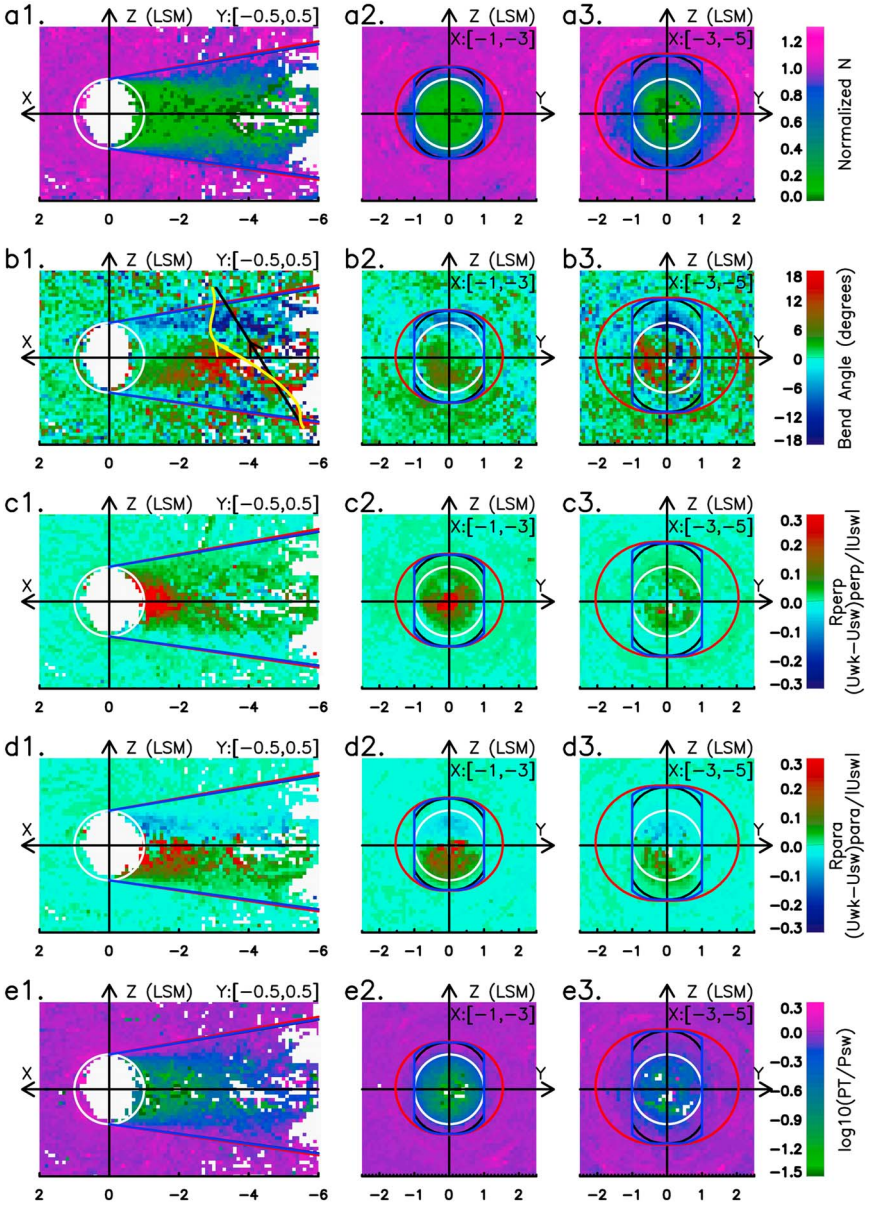

Figure 2. Distributions of the observations from the ARTEMIS satellites in the lunar wake in the *X-Z* plane and in the *Y-Z* plane at different downstream distances. The quantities in the *X-Z* planes (the *Y-Z* planes) are the median values of parameters in each bin with bin size of $dX = 0.1\ R_L$ and $dZ = 0.1\ R_L$ over $Y = [-0.5, 0.5]\ R_L$ ($dY = 0.1\ R_L$ and $dZ = 0.1\ R_L$ over $X = [-1, -3]\ R_L$ and $X = [-3, -5]\ R_L$). (a1-a3) The ion number density normalized by the ion density in the solar wind in the *X-Z* plane (Figure 2a1) and in the *Y-Z* planes at $X = -2\ R_L$ (Figure 2a2) and $X = -4\ R_L$ (Figure 2a3), respectively. (b1–b3) The bend angle of magnetic field line δ_{XZ}. The oblique black line in Figure 2b1 shows the direction of the background IMF $\overrightarrow{B}_{\mathrm{IMF}}$ with $\theta_I = 58°$ (the angle between $\overrightarrow{X}$ and $\overrightarrow{B}_{\mathrm{IMF}}$), and this angle is determined by the averaged direction of IMF in all our data set. The yellow curve schematically depicts the bent field line, and the bend direction is determined by the sign of the bend angle. (c1–c3) The *X* component of the deceleration rate of the perpendicular plasma flow $\overrightarrow{R}_{\mathrm{perp}}$. (d1–d3) The *X* component of the deceleration rate of the parallel plasma flow $\overrightarrow{R}_{\mathrm{para}}$. (e1–e3) The total thermal pressure P_T, which is the sum of the ion and electron pressure. The white circle indicates the solar wind shadow boundary, and the oblique lines or curves mark the locations of the wavefronts of three MHD modes (red indicates the fast mode, black indicates the Alfvén mode, and blue indicates the slow mode) launched at the lunar terminator and propagating at their group velocities in the solar wind.

confined basically within $|Y| < 1\ R_L$. Downstream of the Moon there is a significant density depletion beyond the areas confined by the Alfvén or slow mode fronts but within the fast mode fronts (the blue regions in Figures 2a2 and 2a3). *Zhang et al.* [2014] pointed out that the outermost boundary of the density depletion

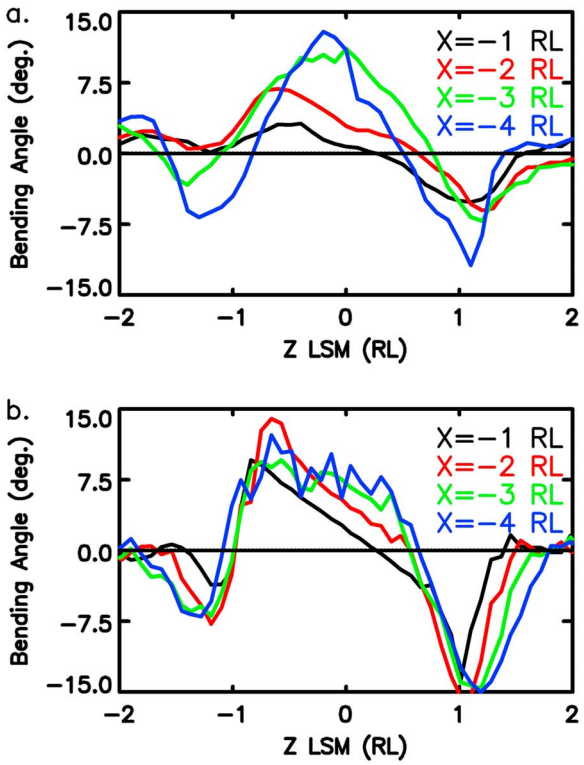

Figure 3. The bend angles of field lines δ_{XZ} plotted as a function of the Z coordinate at different downstream distances. (a) The bend angles observed by the ARTEMIS satellites. (b) The bend angles obtained from the three-dimension hybrid simulation. The color code denotes the different downstream distance.

region is located at the fast mode front. The dimensions in the X direction of the bins are $X=[-1, -3]\ R_L$ and $X=[-3, -5]\ R_L$ for Figures 2a2 and 2a3, respectively. The bin-averaging process has thus obscured the wake boundary, producing density depletion regions (green and blue regions) somewhat smaller than those areas confined by the fast mode fronts at $X=-2\ R_L$ and $X=-4\ R_L$. In addition, the plasma density in the near-Moon central wake is not as low (>0.05) as expected because the data with large measurement uncertainty in velocity and temperature due to extremely low plasma density ($<0.1\ \mathrm{cm}^{-3}$) have been removed from the data set (see *Zhang et al.* [2014] for further information).

Figures 2b1–2b3 display the distribution of the bend angles δ_{XZ} in the X-Z plane and in the Y-Z planes at different downstream distances. The distributions of δ_{XZ} in the X-Z and the Y-Z planes present a clear pattern along Z. Around the lower wake boundary where $Z<-1\ R_L$ and $X<0$ (the narrow blue region in Figures 2b1–2b3), δ_{XZ} is negative; when Z increases from $-1\ R_L$, δ_{XZ} turns positive and above $Z=0\ R_L$ δ_{XZ} begins to decrease; δ_{XZ} finally becomes negative again near the top boundary of the wake (the blue region in Figures 2b1–2b3 where $Z\sim 1\ R_L$ and $X<0$); δ_{XZ} is more strongly negative near the upper wake boundary than near the lower boundary. In order to show the bend angle δ_{XZ} more intuitively, it is plotted as a function of Z at different downstream distances in Figure 3a. It is seen that the profiles of δ_{XZ} versus Z are roughly asymmetric with the following structure: δ_{XZ} dips near $Z=-1.0\ R_L$, and quickly reaches a peak at $Z\sim -0.6\ R_L$; then gradually decreases, becoming negative at $Z\sim 0.6\ R_L$; this is followed by a second dip at $Z\sim 1\ R_L$. The overall profiles of δ_{XZ} along the Z direction show bipolar structures supplemented by small dips near $Z=-1\ R_L$, just as observed in the wake crossing events on 18 August and 28 July in 2011. The bend angle increases with downstream distance (the color code in Figure 3 denotes the downstream distance), which is also consistent with the case studies and with the statistical results of Figure 2. The oblique black line in Figure 2b1 shows the direction of the background IMF $\overrightarrow{B}_{\mathrm{IMF}}$ with $\theta_I=58°$ (the IMF inclination angle shown in the plot is the averaged direction of IMF over our entire data set). The yellow curve schematically shows the bent field line in the wake. Generally speaking, field lines bend as if pulled toward the Moon, although

at the lower wake boundary there is a small region in which field lines bend as if pulled in the downstream direction. Particularly from Figures 2b2 and 2b3, it is found that this field line bend pattern is confined well within $|Y| < 1\ R_L$ region, that is within the slow or Alfvén fronts.

Figures 2c1–2c3 and 2d1–2d3 display the distribution of the X component of the perpendicular and parallel deceleration rates, $R_{perp,X}$ and $R_{para,X}$. $R_{perp,X}$ and $R_{para,X}$ are calculated at all the data points along the wake crossing trajectories. It is seen in Figures 2c1–2c3 that the perpendicular plasma flow is significantly decelerated in the X direction in the near-Moon region ($X > -2\ R_L$) and gradually reaccelerates as the downstream distance increases beyond $X = -2\ R_L$ (Figures 2c1–2c3). For the parallel flow, however, the acceleration in the X direction exhibits an antisymmetric pattern, with field-aligned flow decelerated where $Z < 0$ (Figures 2d1–2d3, the red region) and accelerated where $Z > 0$ (Figures 2d1–2d3, the blue region). This statistical result is consistent with the observations of both events on 18 August 2011 and 28 July 2011. In Figures 2c1–2c3 and 2d1–2d3, the flow perturbations are confined within the slow or Alfvén fronts and the field line bendings are as well.

In order to identify the mechanism that bends the field lines toward the Moon and slows the plasma in the wake, one must investigate pressure balance. Figures 2e1-2e3 show the distribution of the total plasma pressure P_T normalized by the background solar wind thermal pressure (ion pressure plus electron pressure). It is clear that in the near-Moon wake, the pressure is extremely low (the green regions behind the Moon in Figures 2e1-2e3) as a result of blockage of solar wind flow. As plasma returns to the central wake region by flowing along flux tubes, the vertical extent of the low-pressure region gradually diminishes, producing pressure gradients in all three orthogonal directions, $\nabla_X P_T$, $\nabla_Y P_T$, and $\nabla_Z P_T$. In the Y and Z directions, the pressure gradients ($\nabla_Y P_T$ and $\nabla_Z P_T$) point away from the central wake and P_T increases from ~0.4 to 1.0 of the solar wind level within a radial distance less than 1 R_L across the outer wake (Figures 2e2 and 2e3); in the X direction, the gradient ($\nabla_X P_T$) is negative (i.e., pressure increases downstream) because of gradual plasma refilling from regions outside the wake and is much weaker than $\nabla_Y P_T$ or $\nabla_Z P_T$. P_T recovers from an extremely low level in the near-Moon region to ~0.6 of the solar wind level at $X = -6\ R_L$ in the central wake (Figure 2e1).

3. A Three-Dimensional Hybrid Model and Results

Our observations reveal that in the lunar wake there is a moonward pressure gradient force $-\nabla_X P_T$, plasma is decelerated relative to the solar wind flow, and a moonward field bulge develops. All of these perturbations are confined within the slow or Alfvénic wavefronts, giving a hint that there may be an Alfvén wing structure present in the lunar wake. To confirm that these perturbations are indeed Alfvénic, FACs coincident with Alfvén perturbations must be identified. Unfortunately, FACs cannot be obtained from measurements of a single or even two spacecraft; therefore, we have performed a hybrid simulation to identify which perturbations in the wake are Alfvénic and to provide insight into the mechanisms that form the lunar Alfvén wings.

We use a three-dimensional hybrid model of plasma for the Moon [*Holmstrom et al.*, 2012], taking the lunar surface as a perfect plasma absorber and the Moon as a resistive ($10^7\ \Omega$m) obstacle to the solar wind. In hybrid approximations, ions are macroparticles and electrons are a charge-neutralizing fluid. The trajectory of an ion, obtained from $\vec{r}$ and $\vec{v}$, is computed from the equation of motion,

$$\frac{d\vec{v}}{dt} = q\left(\vec{E} + \vec{v}\times\vec{B}\right), \qquad \frac{d\vec{r}}{dt} = \vec{v},$$

where m and q are the ion mass and charge, respectively; $\vec{r}$ and $\vec{v}$ are the position vector and the velocity of the ion, respectively. $\vec{E}$ is the electric field given by

$$\vec{E} = \rho_I^{-1}\left(-J_I\times\vec{B} + \mu_0^{-1}\ \nabla\times\vec{B}\times\vec{B} - \nabla p_e\right) + \eta\mu_0^{-1}\nabla\times\vec{B}$$

and $\vec{B}$ is the magnetic field, calculated from Faraday's law,

$$\frac{\partial\vec{B}}{\partial t} = -\nabla\times\vec{E}$$

where ρ_I is the charge density, J_I is the electric current density carried by ions, p_e is the electron pressure, μ_0 is the permittivity of free space, and η is the resistivity which is zero in the plasma but finite inside the Moon body.

We use the same right-handed coordinate system for simulations and observations where the $+X$ axis points against the solar wind, the $+Y$ axis is determined by $\overrightarrow{B}_{IMF} \times \overrightarrow{X}$, and the Z axis completes the right-hand coordinate system. We place the Moon at the center of the coordinate system, and the solar wind flows along the $-X$ axis and is absorbed by the Moon. We use a simulation domain of size $8 \times 5 \times 5$ R_L^3, with cubic cell size of 0.085 R_L. We use 64 macroparticles per cell and advance the particle trajectories in time steps of 0.001 s. We show simulation results when the model solution has reached a steady state (60 s). The parameters input into the hybrid simulation were the median solar wind properties in our data set given above.

The hybrid simulation well reproduces the observed lunar wake structure, as evident from comparison of Figures 2 and 4 in terms of the parameters of the plasma depletion, bend angle, plasma deceleration, and pressure gradients. The associated FACs is identified in the simulation through Ampere's law $j_{||} = \nabla \times \vec{B} / \mu_0 \cdot \left(\vec{B} / |\vec{B}| \right)$, giving strong support to the conclusion that the field line bending and plasma flow deceleration in the wake are Alfvénic. Notice that the formats of Figures 2 and 4 are the same except for panels b2 and b3. In Figure 4, FACs at $X = -2$ R_L and $X = -4$ R_L, instead of field line bend angles, are shown in panels b2 and b3.

The typical lunar wake feature, a plasma density depletion region expanding in the solar wind frame, is clearly seen in Figures 4a1-4a3. Right behind the Moon, the density is extremely low (dark green region behind the Moon in Figures 4a1-4a3). As plasma refills the wake, the plasma density recovers gradually with increasing downstream distance. By $X = -6$ R_L, the plasma density has recovered to 0.3 of the background solar wind level (in the central wake) and ~0.7 (in outer wake), consistent with satellite observations [*Ogilvie et al.*, 1996; *Zhang et al.*, 2014]. Near the wake boundaries, the locations of the wavefronts of the three MHD modes are shown by curves in red (fast mode), black (Alfvén mode), and blue (slow mode). The color codes are the same as those used in plots of the observations in Figure 2. For the input parameters we chose, the group velocities of three MHD modes are almost the same along the Z directions (parallel to the magnetic field), and it is hard to distinguish which wavefront is associated with the plasma perturbation. However, the slow and Alfvén modes cannot propagate in the $\pm Y$ direction (perpendicular to the magnetic field), and the plasma perturbations (green and blue regions) are clearly confined within the fast mode wavefront, well beyond the Alfvén and slow mode fronts (Figures 4a2 and 4a3), which is consistent with our observations (Figures 2a2 and 2a3).

In the hybrid simulation, field lines indeed bulge toward the Moon after they cross the body. Figure 4b1 shows the distribution of the bend angle δ_{XZ} in the $Y = 0$ plane. Here the definition of the bend angle is that used in our observations: $\delta_{XZ} = \arctan(B_X/B_Z) - \arctan(B_{X,IMF}/B_{Z,IMF})$. The distribution of δ_{XZ} along Z is similar for the simulations in this figure and the observations in Figure 2b1. Around the low wake boundary (the narrow blue region in Figure 4b1 where $Z < -1$ R_L and $X < 0$), δ_{XZ} is negative; when Z increases from -1 R_L, δ_{XZ} turns positive and above $Z = 0$ R_L δ_{XZ} begins to decrease; δ_{XZ} finally becomes negative again near the top boundary of the wake (the blue region in Figure 4b1 where $Z \sim 1$ R_L and $X < 0$); δ_{XZ} is more strongly negative near the upper wake boundary than near the lower boundary. In order to compare the simulations with the statistics obtained from observations, the field line bend angles in the simulation are plotted as functions of Z in Figure 3b, in which the color codes denote the different downstream distances. The simulation reproduces the overall structures of the bend angle well (the magnitude and the asymmetric structure), as is evident from a comparison of Figure 3a (observations) with Figure 3b (simulation). In Figure 3b, the bend angle calculated at -4 R_L shows variations at the same scale as the mesh of the simulation (0.085 R_L), and this could be indicative of numerical artifacts at that distance.

FACs are present in the lunar wake. The FAC distributions in the $X = -2$ R_L and $X = -4$ R_L planes are shown in Figures 4b2 and 4b3. FACs are confined within the Alfvén wavefront, indicating that the magnetic perturbation there are indeed Alfvénic and that an Alfvén wing is present in the lunar wake. The typical magnitude of the FACs in the simulation is about 1–2 nA/m^2. It is noticed that the wake plasma with typical density of ~0.6 cm^{-3} (the normalized density is ~0.1, and the averaged ion density is 6.6 cm^{-3}) in the near-Moon region is reaccelerated by ~75 km/s (corresponding to $R_{perp,X}$ decreasing from 0.3 to 0.1, see cross sections Figures 2c2 and 2c3) within 2 R_L from $X = -2$ R_L to -4 R_L in about 10 s. The corresponding perpendicular current ($\frac{\rho}{|B|}\frac{dU}{dt}$), which is diverted from FACs and acts to reaccelerate the wake plasma, thus should be of a magnitude of ~1.5 nA/m^2 if the field magnitude is 5 nT. One would expect the field-aligned current density to be similar to the estimated perpendicular current density as observed, if the length scales over which the perpendicular and parallel currents flow are

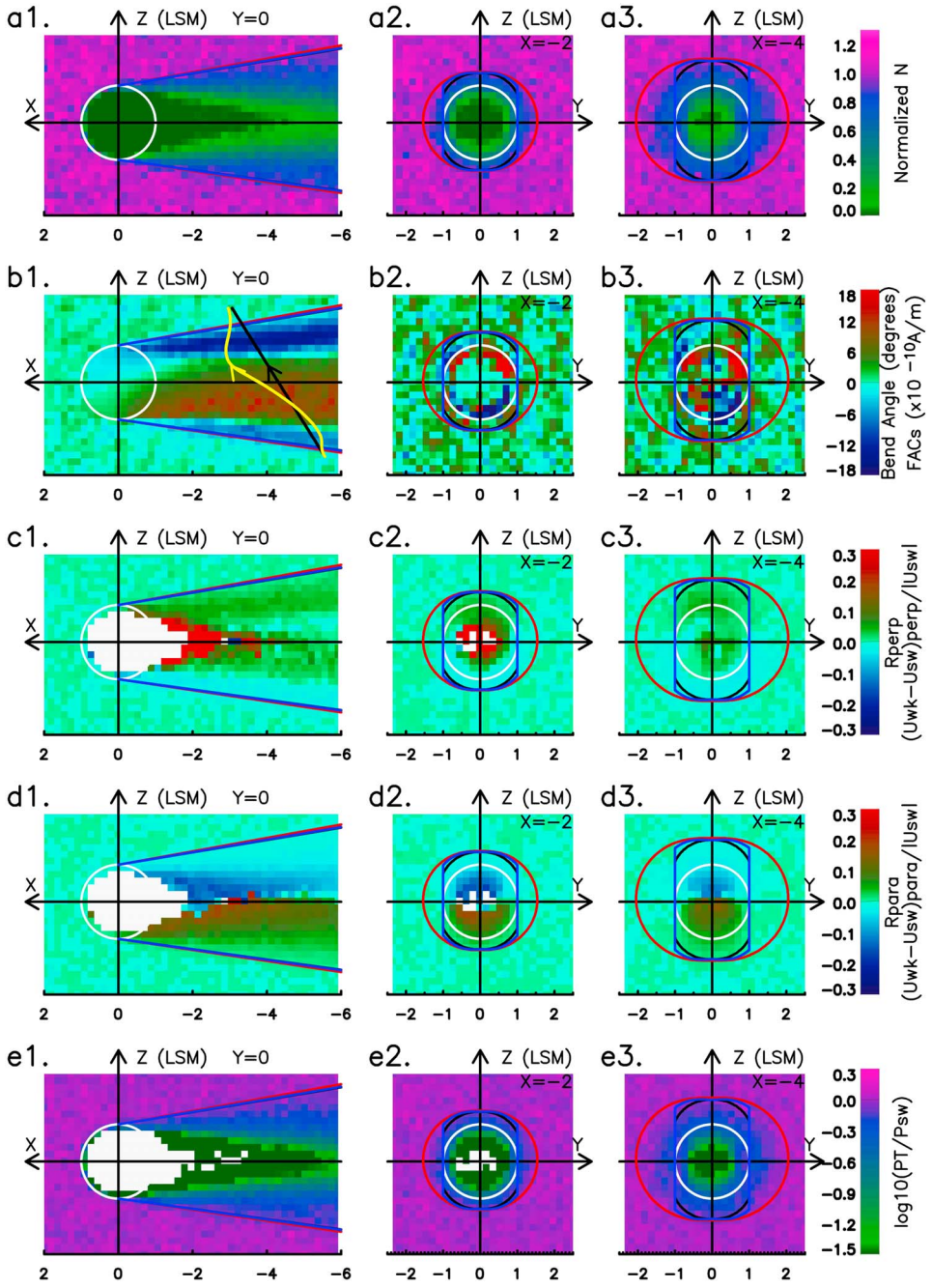

Figure 4. Distributions of the parameters obtained from the three-dimension hybrid simulation. The parameters and formats are the same as Figure 2, except for Figures 4b2 and 4b3. Distributions of FACs at $X = -2\ R_L$ and $X = -4\ R_L$, instead of bend angles, are shown in Figures 4b2 and 4b3.

comparable. FACs are intense near the solar wind shadow boundary. These strong FACs arise from the ambipolar diffusion effect [*Samir et al.*, 1983] and have distorted the Alfvén wing FACs. In the lunar wake, electrons flow down a flux tube to refill the region empty of plasma in the center of the wake, producing a positive FAC on the top of Figures 4b2 and 4b3 and a negative FAC on the bottom.

4. Discussion

Alfvén wings, characterized by flow perturbation, field line bending, and FAC, are a common structure in the interaction between a planetary body and plasma flow. Slowing and diversion of flow are generally thought

to result from the presence of a significant internal magnetic field, the finite conductivity of body itself or its ionosphere [*Drell et al*., 1965], and/or from ion pickup (ionization and charge exchange) [*Goertz*, 1980], and nonconducting, unmagnetized obstacles are generally thought not to generate Alfvén wings. Using theoretical analyses and simulations, *Vernisse et al*. [2013] systematically studied the interaction between stellar winds, whether super-Alfvénic or sub-Alfvénic, and highly resistive planetary bodies. They argued that currents are related to the magnetosonic waves triggered at the surface of the obstacles. By using Cassini data and MHD simulations, *Simon et al*. [2012] confirmed that Alfvén wings are present at Rhea, owing to the diamagnetic current in the wake when Rhea interacts with the sub-Alfvénic Saturn's magnetospheric plasma flow. In this work, we have elucidated the role of both pressure gradient and plasma slowdown in generating the Alfvén wings by performing statistical analyses of simultaneous measurements made by two ARTEMIS satellites, one in the solar wind upstream of the Moon and one in the downstream wake, and by comparing the data with results of a three-dimensional hybrid model of the interaction.

Plasma and magnetic perturbations in the lunar wake should be discussed in two different regions, the deceleration region and the reacceleration region, which are not strictly distinguishable. In the regime of MHD theory, the acceleration/deceleration of plasma is controlled by the momentum equation:

$$\rho \frac{d\vec{V}}{dt} = -\nabla P + \vec{J} \times \vec{B}$$

where ρ, $\vec{V}$, P, $\vec{j}$, and $\vec{B}$ are plasma mass density, velocity, thermal pressure, electric current density and magnetic field, respectively. The lunar wake is taken to be in a steady state ($\rho\partial \rightarrow V/\partial t = 0$), and the inertia term $\rho d\vec{V}/dt$ becomes $\rho\vec{V}\cdot\nabla\vec{V}$. In the near-Moon wake ($X > -2\ R_L$), there are regions where the flow decelerates significantly (red region in Figure 2c1) while field line bend is weak (Figures 2b1 and 2b2 and black and red curves in Figure 3a). In this situation, the magnetic tension force is weak and the moonward pressure gradient force is responsible for plasma deceleration. In the region beyond $X = -2\ R_L$, plasma is reaccelerated from ~$0.7V_{SW}$ to the background solar wind velocity (V_{SW}), and field line bends are clearly seen (Figure 2b1). In this region, the inertial term (spatial variation of velocity in a steady state, $\rho\vec{V}\cdot\nabla\vec{V}$) generates the current. The pressure gradient (∇P, where P is plasma pressure) force also contributes to the field line bend through the perpendicular current ($\vec{j}$). Except for the wake boundary region, the pressure gradient in the X direction $\nabla_X P$ points toward $-X$ as shown by the large green arrow in the center of Figure 5a; at the wake boundary, however, a minor pressure gradient is present in the $+X$ direction between the unperturbed solar wind and the outer wake as shown by the two small green arrows in Figure 5a. Since both the X components of the inertial term ($\rho\vec{V}\cdot\nabla\vec{V}$) and the pressure gradient term (∇P) point mainly downstream, the net perpendicular current and the associated field line bend are large in this region and the pressure gradient is taken as an example to interpret how the associated current bend field lines in Figures 5a and 5b. The diamagnetic currents arising from these pressure gradients $\vec{j}_{\nabla PX} = \left(-\nabla_X P \times \vec{B}\right)/B^2$ point inward in the central wake along the $-Y$ direction and point outward on the wake boundary as shown by the red symbols in Figure 5 a, and these currents make magnetic field perturbations in the $-X$ direction where $Z > 0$ and in the $+X$ direction where $Z < 0$ as shown by the pink arrows in Figure 5a. The background IMF field line (the blue arrow in Figure 5a) is thus bent toward the Moon as shown by the cyan curve with arrowhead in Figure 5a. These currents produce a quasi-antisymmetric profile of δ_{XZ} along Z (red curve in Figure 5b).

Additional features of the field bends and the flow require further interpretation. In the lunar Alfvén wings, field line bending is asymmetric in Z both in the observations and in the hybrid simulation (Figures 3a and 3b). The asymmetry is a combined effect of the tilted field line and the presence of density and thermal pressure gradients along the Z direction ($\nabla_Z P$). The associated diamagnetic currents (red arrows in Figure 5c) make a bipolar perturbation to the background IMF as shown by the cyan curve with arrow in Figure 5c (the pink arrows show the magnetic perturbations). The bend angle profile along the Z direction associated with $\nabla_Z P$ is shown schematically by the red curve in Figure 5d, with two negative dips (clockwise rotation of field lines) near the wake boundaries but a positive perturbation (anticlockwise rotation) in the central wake. The profile of the resulting bend angle δ_{XZ} is the combination of the effects of $\nabla_X P$ and $\nabla_Z P$, which is shown schematically by the blue curve in Figure 5d. This schematic form is a good representation of what is seen in our observations as well as in the hybrid simulation.

The flow deceleration also exhibits asymmetry along the Z axis (black curves in Figures 1a3 and 1b3). Flow in the upper half of the wake ($Z > 0$) is decelerated less than that in the lower half ($Z < 0$), and plasma is even

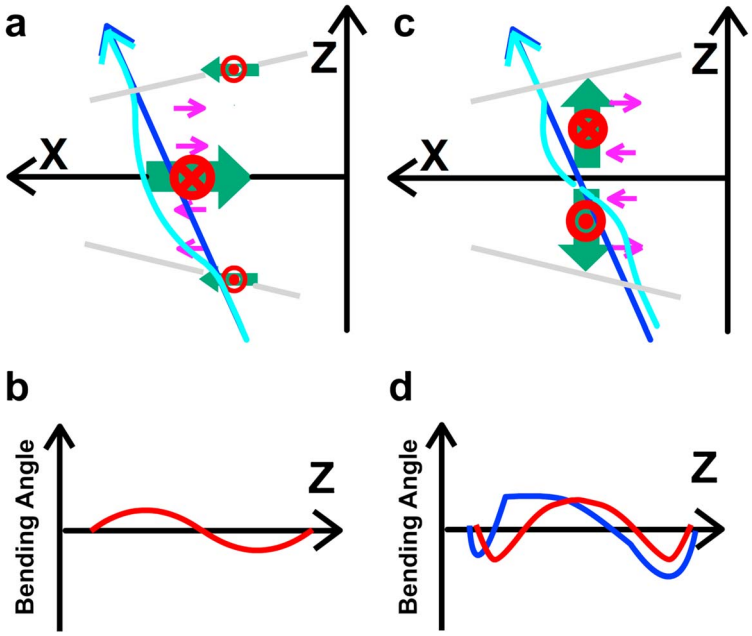

Figure 5. (a) Diagram in the $Y = 0$ plane depicting the sense of the pressure gradients along the lunar wake (green arrows), the associated diamagnetic currents (red symbols with X denoting into the plane and a dot denoting out of the plane), and the magnetic perturbation directions (pink arrows). The blue arrow represents a field line of the background IMF, and the cyan curve with arrow denotes a perturbed magnetic field line. The gray lines demark the wake boundaries. (b) In red, the bend angle (idealized) caused by pressure gradients along the lunar wake plotted as a function of Z. (c and d) Schematically the bending effects of a pressure gradient along Z with the same colors scheme as used for Figure 5a. The blue curve in Figure 5d shows schematically the net bends of a field line caused by combining effects of pressure gradients along the lunar wake (X component) and perpendicular to the lunar wake (Z component).

accelerated at $Z > 0$ (panels a3 and b3 in Figure 1 and panels d1–d3 in Figures 2 and 4). We attribute this asymmetry in plasma flow deceleration to the effects of plasma refilling along field lines from the surrounding solar wind into the wake [*Ogilvie et al*., 1996; *Gharaee et al*., 2015]. On average, the IMF in our data set tilts, as shown by the oblique black line in Figure 2b; the angle θ_I between $\overrightarrow{X}$ and $\overrightarrow{B}_{\mathrm{IMF}}$ is ~58°. In this geometry, when plasma refills the wake along field lines from above, the plasma velocity in the $-X$ direction increases; when plasma refills from below, the plasma velocity in the $-X$ direction decreases (panels d1–d3 in Figures 2 and 4). The superposition of the antisymmetric parallel flow and the symmetric perpendicular flow produces the observed asymmetry.

Unlike a widely open wing structure at the planetary moons, the lunar Alfvén wings that form in the solar wind are confined within an acute angle of the Mach cone due to the super-Alfvénic solar wind. The two wings appear strongly "folded-back". The configuration of an Alfvén wing structure depends on the flare angle of the two wings, and for a simplest case (the background magnetic field is perpendicular to the background flow), it is defined by $\theta_A = \mathrm{atan}(1/M_A)$, where $M_A = V/V_A$, V is the background flow velocity and V_A is Alfvén velocity [*Ridley*, 2007]. In the lunar wake Alfvén wing case, the Z component of the Alfvén velocity is $V_A = \sin\theta_I \sqrt{B^2/m_i n_i \mu_0}$, where θ_I is the IMF direction relative to the X direction, B is the magnitude of the IMF, m_i is the ion mass, and n_i is the ion number density. The median values in our data set give $V_A = 64$ km/s. The background solar wind velocity ($V = 370$ km/s) is much higher than the Alfvén velocity, and thus, the solar wind is super-Alfvénic. In our data, the Alfvén wing flaring angle θ_A is very small (about 8°).

In a previous analysis, we speculated that the deceleration of flow and the bending of the field in the wake could be produced by interaction with heavy lunar dust grains, roughly stationary in the Moon's frame [*Zhang et al*., 2014]. It is known that the Moon is surrounded by a tenuous atmosphere of charged dust grains. Direct evidence for these grains is the existence of the so-called "lunar horizon glow" [e.g., *Rennilson and Criswell*, 1974], which is thought to arise from the scattering of sunlight off of the dust grains [*Zook and*

McCoy, 1991]. The charged dust is present on both dayside and nightside of the Moon at altitudes up to 100 km above the lunar surface [e.g., *Stubbs et al*., 2006]. The 3-D hybrid simulation that we have described in this work was run without lunar dust but, nonetheless, reproduced our observations. Both observations and simulations identify a pressure gradient along the lunar wake sufficiently large to produce the effects observed, and the simulation shows that Alfvénic perturbations and associated closure current system are significant in producing both bends and flow reacceleration in the wake. Thus, it seems that charged dust need not be invoked to explain the dominant measured properties of the lunar wake, although perturbations related to charged dust may yet be found to affect some aspects of the field and plasma structure near the Moon.

5. Summary

Alfvén wings usually develop from the interaction between conducting or magnetized obstacles and a flowing plasma. Incompressible perturbations are imposed by field-aligned currents closing through the conducting body, which reaccelerate the slowed plasma [*Neubauer*, 1980; *Kivelson et al*., 1997]. Finite conductivity of the interaction system may arise from the body itself or the surrounding plasma of the body (ionosphere) [*Neubauer*, 1980; *Linker et al*., 1998]. The interactions between moving plasma and static heavy ions (charged dust) or pickup ions added in the vicinity of the body provide other possible sources for the generation of Alfvén wings [*Linker et al*., 1998; *Jia et al*., 2011]. In the literature, Alfvén wings have only rarely been identified or discussed in the interaction of nonconducting obstacles and flowing plasma [*Khurana et al*., 2008; *Simon et al*., 2012; *Vernisse et al*., 2013]. However, theoretical analysis and simulations predict that diamagnetic currents, which arise from pressure gradients, may be significant sources for magnetic perturbations in a lunar-type interaction between stellar winds, whether super-Alfvénic or sub-Alfvénic, and highly resistive planetary bodies [*Vernisse et al*., 2013]. By using Cassini data, *Simon et al*. [2012] showed that Alfvén wings are present in the lunar-type interaction system between the sub-Alfvénic magnetospheric plasma flow of Saturn and its moon, Rhea, and ascribed their presence exclusively to the diamagnetic currents. In this paper, an analysis of measurements made simultaneously by two ARTEMIS satellites, one in the solar wind upstream of the Moon and one in the downstream wake, and comparison of the data with results of three-dimensional hybrid model of the interaction reveal that pressure gradients in the wake slow down the inflowing solar wind. An Alfvén wing current system is generated in response in the super-Alfvénic plasma system that reaccelerates the wake plasma to the ambient solar wind speed. Such Alfvén wing structures, caused by pressure gradients and the attendant plasma slowdown in the wake, should exist downstream of any nonconducting body in a super-Alfvénic plasma flow.

ARTEMIS satellites identified two basic features of Alfvén wings in the lunar wake: bending of the magnetic field (producing a Moonward-oriented bulge in the field near the center of the wake) and deceleration of plasma flow. Observations show that these two perturbations are confined within slow or Alfvén fronts (panels b1–b3 and c1–c3 in Figures 2 and 4). We ruled out the possibility that these field line bulges are caused by finite conductivity of the Moon itself as suggested by *Wang et al*. [2011], noting that field line bending caused by body induction should decay in the wake. In our data, however, the bend angles of field lines increase as the downstream distance increases (Figures 1a2 and 1b2 and Figures 2b1–2b3).

The simulations well represent all the lunar wake properties observed by ARTEMIS satellites: the lunar wake identified by the depletion of plasma density is confined by fast mode wavefronts; the field line bend angle δ_{XZ} and flow deceleration are confined by the Alfvénic or the slow mode fronts. FACs associated with these perturbations in the simulations confirm the presence of Alfvén wings in the lunar wake.

Acknowledgments
This work was supported by the National Science Foundation of China (41274171) and the Chinese Academy of Sciences project (KZZD-EW-01-3). Work at UCLA was supported by NASA through THEMIS 443869-TM-22620 and THEMIS/ARTEMIS project through NAS5-02099. All of the data used in this work were obtained from the ARTEMIS website http://themis.ssl.berkeley.edu. We also specially acknowledge with appreciation K.H. Glassmeier, U. Auster, and W. Baumjohann for the use of FGM data provided under the lead of the Technical University of Braunschweig and with financial support through the German Ministry for Economy and Technology and the German Center for Aviation and Space (DLR) under contract 50 OC 0302.

References

Angelopoulos, V. (2011), The ARTEMIS mission, *Space Sci. Rev.*, doi:10.1007/s11214-010-9687-2.

Auster, H. U., et al. (2008), The THEMIS fluxgate magnetometer, *Space Sci. Rev.*, *141*, 235–264, doi:10.1007/s11214-008-9365-9.

Clack, D., J. C. Kasper, A. J. Lazarus, J. T. Steinberg, and W. M. Farrell (2004), Wind observations of extreme ion temperature anisotropies in the lunar wake, *Geophys. Res. Lett.*, *31*, L06812, doi:10.1029/2003GL018298.

Colburn, D. S., R. G. Currie, J. D. Mihalov, and C. P. Sonett (1967), Diamagnetic solar-wind cavity discovered behind moon, *Science*, *158*, 1040–1042, doi:10.1126/science.158.3804.1040.

Drell, S., H. Foley, and M. Ruderman (1965), Drag and propulsion of large satellites in the ionosphere: An Alfvén propulsion engine in space, *J. Geophys. Res.*, *70*, 3131–3145, doi:10.1029/JZ070i013p03131.

England, A. W., G. Simmons, and D. Strangway (1968), Electrical conductivity of the Moon, *J. Geophys. Res.*, *73*(10), 3219–3226, doi:10.1029/JB073i010p03219.

Fatemi, S., M. Holmstrom, Y. Futaana, S. Barabash, and C. Lue (2013), The lunar wake current systems, *Geophys. Res. Lett.*, *40*, 17–21, doi:10.1029/2012GL054635.
Gharaee, H., R. Rankin, R. Marchand, and J. Paral (2015), Properties of the lunar wake predicted by analytic models and hybrid-kinetic simulations, *J. Geophys. Res. Space Physics*, *120*, 3795–3803, doi:10.1002/2014JA020907.
Goertz, C. K. (1980), Io's interaction with the plasma torus, *J. Geophys. Res.*, *85*, 2949–2956, doi:10.1029/JA085iA06p02949.
Halekas, J. S., Y. Saito, G. T. Delory, and W. M. Farrell (2011), New views of the lunar plasma environment, *Planet. Space Sci.*, *59*(14), 1681–1694, doi:10.1016/j.pss.2010.08.011.
Halekas, J. S., Brain, D. A., and Holmström, M. (2015), Moon's plasma wake, in *Magnetotails in the Solar System*, edited by A. Keiling, C. M. Jackman, and P. A. Delamere, chap. 9, pp. 149–167, John Wiley, Hoboken, N. J., doi:10.1002/9781118842324.
Hoffman, J. H., R. R. Hodges Jr., F. S. Johnson, and D. E. Evans (1973), Lunar atmospheric composition results from Apollo 17 Proc. Lunar Planet. Sci. Conf. 4th, 2865–2875.
Holmstrom, M., S. Fatemi, Y. Futaana, and H. Nilsson (2012), The interaction between the Moon and the solar wind, *Earth Planets Space*, *64*, 237–245, doi:10.5047/eps.2011.06.040.
Jia, X., R. Walker, M. Kivelson, K. Khurana, and J. Linker (2009), Properties of Ganymede's magnetosphere inferred from improved three-dimensional MHD simulations, *J. Geophys. Res.*, *114*, A09209, doi:10.1029/2009JA014375.
Jia, Y.-D., Y. J. Ma, C. T. Russell, H. R. Lai, G. Toth, and T. I. Gombosi (2011), Perpendicular flow deviation in magnetized counter-streaming plasma, *Icarus*, *218*(2), 895–905, doi:10.1016/j.icarus.2012.01.017.
Khurana, K. K., C. T. Russell, and M. K. Dougherty (2008), Magnetic portraits of Tethys and Rhea, *Icarus*, *193*, 465–474, doi:10.1016/j.icarus.2007.08.005.
Kivelson, M. G., K. K. Khurana, F. V. Coroniti, S. Joy, C. T. Russell, R. J. Walker, J. Warnecke, L. Bennett, and C. Polanskey (1997), The magnetic field and magnetosphere of Ganymede, *Geophys. Res. Lett.*, *24*(17), 2155–2158, doi:10.1029/97GL02201.
Kopp, A., and Ip, W.-H. (2002), Resistive MHD simulations of Ganymede's magnetosphere 2. Time variabilities of the magnetic field topology, *J. Geophys. Res.*, *107*(A12), 1490, doi:10.1029/2001JA005071.
Linker, J. A., K. K. Khurana, M. G. Kivelson, and R. J. Walker (1998), MHD simulations of Io's interaction with the plasma torus, *J. Geophys. Res.*, *103*(E9), 19,867–19,877, doi:10.1029/98JE00632.
Lyon, E. F., H. S. Bridge, and J. H. Binsack (1967), Explorer 35 plasma measurements in the vicinity of the moon, *J. Geophys. Res.*, *72*(23), 6113–6117, doi:10.1029/JZ072i023p06113.
McFadden, J. P., C. W. Carlson, D. Larson, M. Ludlam, R. Abiad, B. Elliott, P. Turin, M. Marckwordt, and V. Angelopoulos (2008), The THEMIS ESA plasma instrument and in-flight calibration, *Space Sci. Rev.*, *141*, 277–302, doi:10.1007/s11214-008-9440-2.
Ness, N. F., K. W. Behannon, C. S. Searce, and S. C. Cantarano (1967), Early results from the magnetic field experiment on lunar Explorer 35, *J. Geophys. Res.*, *72*(23), 5769–5778, doi:10.1029/JZ072i023p05769.
Neubauer, F. (1980), Nonlinear standing Alfvén wave current system at Io: Theory, *J. Geophys. Res.*, *85*, 1171–1178, doi:10.1029/JA085iA03p01171.
Ogilvie, K. W., J. T. Steinberg, R. J. Fitzenreiter, C. J. Owen, A. J. Lazarus, W. M. Farrell, and R. B. Torbert (1996), Observations of the lunar plasma wake from the WIND spacecraft on December 27, 1994, *Geophys. Res. Lett.*, *23*(10), 1255–1258, doi:10.1029/96GL01069.
Rennilson, J. J., and D. R. Criswell (1974), Surveyor observations of lunar horizon glow, *Moon*, *10*, 121–142, doi:10.1007/BF00655715.
Ridley, A. J. (2007), Alfvén wings at Earth's magnetosphere under strong interplanetary magnetic fields, *Ann. Geophys.*, *25*, 533–542, doi:10.5194/angeo-25-533-2007.
Saito, Y., et al. (2008), Solar wind proton reflection at the lunar surface: Low energy ion measurements by MAP-PACE onboard SELENE (KAGUYA), *Geophys. Res. Lett.*, *35*, L24205, doi:10.1029/2008GL036077.
Samir, U., K. H. Wright Jr., and N. H. Stone (1983), The expansion of a plasma into a vacuum: Basic phenomena and processes and applications to space plasma physics, *Rev. Geophys.*, *21*, 1631–1646, doi:10.1029/RG021i007p01631.
Simon, S., H. Kriegel, J. Saur, A. Wennmacher, F. M. Neubauer, E. Roussos, U. Motschmann, and M. K. Dougherty (2012), Analysis of Cassini magnetic field observations over the poles of Rhea, *J. Geophys. Res.*, *117*, A07211, doi:10.1029/2012JA017747.
Sonett, C. P., D. S. Colburn, and R. G. Currie (1967), The intrinsic magnetic field of the Moon, *J. Geophys. Res.*, *72*(21), 5503–5507, doi:10.1029/JZ072i021p05503.
Southwood, D. J., M. G. Kivelson, R. J. Walker, and J. A. Slavin (1980), Io and its plasma environment, *J. Geophys. Res.*, *85*, 5959–5968, doi:10.1029/JA085iA11p05959.
Stubbs, T. J., R. R. Vondrak, and W. M. Farrell (2006), A dynamic fountain model for lunar dust, in *Moon and Near-Earth Objects*, edited by P. Ehrenfreund, B. Foing, and A. Cellino, pp. 59–66, Elsevier Science Bv, Amsterdam.
Vernisse, Y., H. Kriegel, S. Wiehle, U. Motschmann, and K.-H. Glassmeier (2013), Stellar winds and planetary bodies simulations: Lunar type interaction in super-Alfvenic and sub-Alfvenic flows, *Planet. Space Sci.*, *84*, 37–47, doi:10.1016/j.pss.2013.04.004.
Wang, Y. C., J. Muller, W.-H. Ip, and U. Motschmann (2011), A 3D hybrid simulation study of the electromagnetic field distributions in the lunar wake, *Icarus*, *216*(2), 415–425, doi:10.1016/j.icarus.2011.09.021.
Whang, Y. C., and N. F. Ness (1970), Observations and interpretation of lunar mach cone, *J. Geophys. Res.*, *75*(31), 6002–6010, doi:10.1029/JA075i031p06002.
Xie, L. H., L. Li, Y. T. Zhang, and D. L. De Zeeuw (2013), Three-dimensional MHD simulation of the lunar wake, *Sci. China-Earth Sci.*, *56*(2), 330–338, doi:10.1007/s11430-012-4383-6.
Zhang, H., K. K. Khurana, M. G. Kivelson, V. Angelopoulos, W. X. Wan, L. B. Liu, Q.-G. Zong, Z. Y. Pu, Q. Q. Shi, and W. L. Liu (2014), Three-dimensional lunar wake reconstructed from ARTEMIS data, *J. Geophys. Res. Space Physics*, *119*, 5220–5243, doi:10.1002/2014JA020111.
Zook, H. A., and J. E. McCoy (1991), Large-scale lunar horizon glow and a high altitude lunar dust exosphere, *Geophys. Res. Lett.*, *18*, 2117–2120, doi:10.1029/91GL02235.